Toward Ultralight High Strength Structural Materials via Collapsed Carbon Nanotube Bonding

Benjamin D. Jensen[1], Jae-Woo Kim[2], Godfrey Sauti[1], Kristopher E. Wise[1], Liang Dong[3], Haydn N.G. Wadley[3], Emilie J. Siochi[1]

[1]Advanced Materials and Processing Branch, NASA Langley Research Center, Hampton, VA 23681

[2]National Institute of Aerospace, Hampton, VA 23666

[3]Department of Materials Science and Engineering, University of Virginia, Charlottesville, VA 22904

Abstract

The growing commercial availability of carbon nanotube (CNT) macro-assemblies such as sheet and yarn is making their use in structural composite components increasingly feasible. However, the mechanical properties of these materials continue to trail those of state-of-the-art carbon fiber composites due to relatively weak inter-tube load transfer. Forming covalent links between adjacent CNTs promises to mitigate this problem, but it has proven difficult in practice to introduce them chemically within densified and aligned CNT materials due to their low permeability. To avoid this limitation, this work explores the combination of pulsed electrical current, temperature, and pressure to introduce inter-CNT bonds. Reactive molecular dynamics simulations identify the most probable locations, configurations, and conditions for inter-nanotube bonds to form. This process is shown to introduce covalent linkages within the CNT material that manifest as improved macroscale mechanical properties. The magnitude of this effect increases with increasing levels of pre-alignment of the CNT material, promising a new synthesis pathway to ultralight structural materials with specific strengths and stiffnesses exceeding 1 and 100 GPa/(g/cm^3), respectively.

Introduction

Future space exploration missions require new generations of ultra-lightweight structural materials to reduce the energy requirements for payload delivery throughout the solar system. Systems-level analyses have shown that materials with higher ratios of strength to mass than are currently available are required to enable implementation of more ambitious concepts for future missions.[1] The sp^2 bonded form of carbon found in graphene and carbon nanotubes (CNTs) results in an in-plane Young's modulus of 1,000 GPa and a tensile strength above 100 GPa for a defect free form.[2,3] These extremely high nanoscale tensile properties have led to significant interest in their use for structural materials. While bulk CNTs in formats such as sheets and yarns are now commercially available in quantities sufficient to manufacture small flight articles,[4] their mechanical properties are governed by load transfer *between* the tubes, and have orders of magnitude lower moduli and strengths.[5] Current graphene and CNT materials do not have mechanical performance sufficient to displace existing materials in aerospace structures.

Processing strategies to improve the mechanical properties of CNT sheet and yarn have generally involved some combination of alignment and densification[6–10] followed by chemical modification, using, for example, polymers, crosslinking molecules, or irradiation.[11–19] Alignment and densification have produced the largest mechanical property improvements. In densified and aligned materials, load transfer could be improved further by the addition of covalent links between adjacent CNTs.[20–22] However, in this format, the material is essentially impermeable, and infiltration driven processes effectively yield only surface treatments. In order to achieve the load transfer that capitalizes on the nanoscale mechanical properties of CNTs, it is necessary to create linkages within densified and aligned CNT materials.

In a departure from conventional infiltration dependent processing approaches, the work described here uses a combination of pulsed electric current, high temperature, and a low applied pressure to induce the formation of covalent links between CNTs within a partially aligned CNT sheet. Although a continuous process will eventually be needed for high-volume production, a (batch process) spark plasma sintering (SPS) method is

used to understand the role of these process parameters upon the covalent linking process and resulting mechanical properties. SPS has been used extensively to sinter powdered metals and ceramics,[23] as well as CNTs in a loose-powder format.[24–27] While previous reports demonstrated the formation of covalent links in loose-powder CNT sintered compacts,[25–28] the starting materials had poor microstructure and the resulting mechanical properties were too low to be useful for aerospace structures.[24,29–34] In contrast to CNT powder, which has essentially no strength before processing, the commercially available sheet material used in this work has a better microstructure resulting in a specific strength in the hundreds of MPa/(g/cm^3) before processing.[9,35] Subjecting these materials to a range of combined stimuli possible with SPS resulted in physical behavior that suggested load transfer between CNTs was improved. Experimental confirmation of chemical changes was carried out using X-ray diffraction, Raman spectroscopy, and high-resolution transmission electron microscopy (HR-TEM). Reactive molecular dynamics (MD) simulations provided insight into the mechanisms, optimum processing conditions, and structures that promote inter-CNT bond formation.

Results

Inter-CNT bond formation

The CNT sheets were composed primarily of double-walled tubes with a typical diameter of 7 - 8 nm which are more stable in a collapsed configuration.[36] The CNTs had agglomerated into bundles to form a fibrous network microstructure visible in Figure 1(a). In the pristine material, no bundle alignment was observed. Stretching the CNT sheet material results in alignment in the stretch direction, as shown in Figure 1(b). To investigate the mechanisms of molecular rearrangement, simplified experimental structures were modeled using reactive MD simulation with the reactive force field ReaxFF.[37,38] These simulations were used to predict the covalent structural changes to collapsed CNTs in relation to pressure and temperature. The simulations do not address the possible independent role of electric current flow and simulation of all aspects of the experimental SPS process remained beyond the scope of current simulations. Isotherms were created at several temperatures by

gradually increasing the pressure in the simulation cells while holding the temperature constant. To assess their stability, newly-formed bonds were investigated after returning to ambient temperature and pressure.

The progression of simulated structural changes for parallel CNT configurations [Figure S1(a)] is shown in Figure 1(d) and the corresponding simulated phase diagram is shown in Figure 1(c). The simulations reveal that the initial bond formation events, regardless of temperature or pressure, occur at the high curvature side-loops of the collapsed CNTs. Strain in the high-curvature regions of collapsed CNTs induces rehybridization of their sp^2-hybridized orbitals to a configuration with greater sp^3 character.[39] As the pressure increases, the curvature of the side-loops increases further while also driving these more "reactive atoms" on adjacent CNTs closer together. Eventually, bond formation becomes an energetically favorable process. Once sparse covalent links are initiated, the high-curvature regions relax their strain energy by transforming into sp^3-carbon rich structures (at lower temperature) or planar graphitic structures (at higher temperature) with further increases in either pressure or temperature. At the highest pressures, cubic diamond formation occurred in planar regions of the collapsed CNTs.

Figure 2(a) shows a HR-TEM image of a CNT sheet that was processed using SPS. As previously observed in TEM imaging of pristine CNT sheets,[8,40] the collapsed CNTs are packed into columnar stacks. The crystal packing of the collapsed CNTs is somewhat disrupted by the presence of a smaller-diameter round CNT. Figure 2(b) shows a region of sp^3-carbon rich simulation structure for comparison. An enlarged HR-TEM image from another location in the sample is shown in Figure 2(c). The arrows mark locations where the CNTs are separated by less than the typical van der Waals bond distance of 0.34 nm. While bonding cannot be unambiguously assigned on the basis of the HR-TEM image, it clearly bears a resemblance to the side-loop bonding found in the similarly scaled simulation image shown in Figure 2(d).

Although there are unavoidable challenges in directly comparing the simulation and experimental conditions, there are instructive lessons that can be drawn from these results. The simulations show that the most probable location of covalent bond formation is at the curved side-loops of collapsed CNTs and that a processing

condition window for the formation of these bonds exists, and therefore covalent bond formation may be experimentally controllable. The simulations show that this window is upper-bounded by the formation of diamond and graphite if critical pressures or temperatures, respectively, are surpassed. Maximizing mechanical properties will require optimizing the extent of inter-CNT bond formation while minimizing material domains that cross over into the diamond or graphitic regions of the phase diagram.

Influence of processing conditions

The SPS process was controlled to produce systematic variations of a target temperature in graphite dies and target pressures applied to CNT sheet samples contained within them. While these macroscopic conditions will simply be referred to as SPS pressure and SPS temperature, it is important to note that localized pressure and temperature domains within the sample are expected to vary substantially both spatially within the sample and with processing time. Time dependent variation in temperature is due to the rapid pulsing of the electrical current. Spatial variations are expected to result from current percolation through the CNT array resulting in localized joule heating from variations in the CNT packing. These are also capable of inducing additional inhomogeneities in pressures from locally higher out-of-plane modulus and thermal expansion. These inhomogeneities complicate direct comparison between the simulation and experimental conditions. Even though they cannot be measured directly, local domains in the material may experience higher pressures and temperatures comparable to those in the MD simulations. Diamond crystals, which have been observed after SPS processing, can be as large as 10 μm,[41] and are consistent with being markers of local domains where local conditions greatly exceeded the nominal applied SPS pressure and temperature. Some have speculated that nonthermal electrical effects may also contribute to the formation of higher energy structures like diamond,[42] although this is not considered in the simulations in this work.

The simulations predict that exceeding the upper temperature or pressure boundary for covalent bond formation results in the formation of graphitic or diamond structures, respectively. X-ray diffraction (XRD) spectroscopy was used to detect the presence of diamond and graphitic crystalline phases in pristine and SPS processed CNT

sheets [Figure 3(a)]. After SPS processing, peaks associated with n-diamond ($2\theta = 51^{\circ}$) and cubic diamond ($2\theta = 75^{\circ}$ and 91°) were observed. These observations agree well with previous studies of SPS processed CNT powders, where n-diamond and cubic diamond XRD peaks were observed in samples in which small diamond crystals were also identified with transmission electron microscopy, scanning electron microscopy, and Raman spectroscopy.[41,43] In addition to the formation of diamond after SPS processing, the graphite peak ($2\theta = 55^{\circ}$) increased, indicating some graphitization also occurred during the SPS process. While graphitic and diamond phases are not the desired structures, it is encouraging that the SPS process appears to be more than capable of producing the conditions for covalent bond formation, despite the low SPS pressure. Comparing the samples processed at SPS pressures of 0 (the lowest marginal contact pressure) and 40 MPa at the same SPS temperature of 1,000 ˚C, small diamond peaks are observed in the 0 MPa sample and are similar or perhaps slightly smaller for the 40 MPa sample. The observation of diamond peaks in the uncompressed sample indicates that the globally applied SPS pressure is not the source of pressure driving diamond formation. The diamond peaks increase with the SPS temperature, which is interdependent with the electrical current pulses, indicating that this is likely the driving force for diamond formation.

Since the creation of covalent links to the sidewall of a CNT disrupts the crystalline structure of the tube, it produces shifts in frequency and intensity of their characteristic vibrational modes.[44] Raman spectroscopy is therefore an excellent means of tracking these changes, and provides a qualitative description of the disorder in the CNT structure. Specifically, an increasing intensity ratio of the D peak (1,299 cm^{-1}) to the G peak (1,574 cm^{-1}) indicates increasing disruption of the CNT structure. As shown in Figure 3(b), the intensity ratio between the D and G peaks increases with increases in both the SPS temperature and SPS pressure. This indicates increasing disruption of the CNTs with increasingly aggressive SPS processing conditions, consistent with the formation of bonds between adjacent tubes. The G peak frequency is also up-shifted after SPS processing, which may indicate the formation of graphite during SPS processing, in agreement with the XRD spectra.

The tensile mechanical response of pristine and SPS processed samples is shown in Figure 3(c). The low Young's modulus and very high nonlinear strain prior to failure observed in the pristine and low SPS temperature processed material is consistent with a tube sliding mechanism. If load transfer between CNTs relative to their length is insufficient for the transferred stress to reach the tensile fracture stress of the CNTs, they are able to slide against each other, resulting in a high nonlinear failure strain. Figure 3(c) clearly shows that SPS processing substantially reduces the failure strain, consistent with improved load transfer between CNTs. The sample processed with no compression had a much higher Young's modulus and retained about a half of the plasticity of the pristine sample, but at a substantially higher flow stress. Stress-strain curves for samples processed at non-zero SPS pressures do not show this high failure strain, an indication that CNT sliding has been greatly reduced or eliminated. The highest SPS temperature of 1,500 ˚C resulted in an extremely brittle material that failed at the lowest strain. These results indicate that SPS processing can improve load transfer between CNTs and that SPS conditions can be adjusted to produce a tailored mechanical response.

Figure 3(d) shows the specific stiffnesses and specific tensile strengths of the samples in Figure 3(c) plotted as a function of density. Interestingly, the specific strength and stiffness of the sample processed at a pressure of 0 MPa increased despite a decrease in density. It is also notable that the two independent samples processed at 1,000 ˚C and 40 MPa exhibited very similar specific strength and stiffness despite differing densities. These results indicate that densification is not the primary factor improving the mechanical performance and suggest the involvement of inter-tube bonding. While the specific stiffness continues to increase weakly with density, the specific strength initially increases but falls at higher densities which also correspond to more aggressive processing conditions.

Influence of CNT alignment

If inter-tube bonds preferentially form at the curved side-loops of collapsed CNTs, as indicated by the simulations and HR-TEM observations, alignment of the CNT sheet samples prior to SPS processing should lead to improved mechanical properties of the resulting material. Stretching the as-received CNT sheet material rotates and aligns

the CNTs in the direction of the applied stretch. Because the results in the previous section showed that SPS processing conditions of 1,000 ˚C and 40 MPa were sufficient to induce inter-tube bonding without over-producing diamond or graphite, these parameters were used for all aligned samples.

Representative stress-strain responses for a series of increasingly stretched (pre-strained) samples are compared in Figure 4(a) and specific strengths and moduli are shown in Figure 4(b). Increasing CNT alignment in the material decreases the failure strain while increasing the strength and modulus, as has been reported elsewhere.[9] Application of SPS processing to the aligned samples further increases specific strengths and stiffnesses and decreases the failure strain for all levels of pre-strain. In contrast to the aligned but unprocessed samples, the failure strain of the SPS processed samples increased with increasing alignment. This indicates that toughness is improved by combining alignment with SPS processing, relative to SPS processing alone.

Increasing alignment and densification reduces the effectiveness of infiltration-based processing strategies. For the SPS processing reported here, however, Figure 4(b) illustrates that this behavior is reversed. Both the specific stiffnesses and strengths increase more rapidly with alignment in the SPS processed samples than in the unprocessed samples. The highest specific strength and stiffness observed in this work resulted from SPS treatment of the 43% pre-strained sample, resulting in a specific strength of 973.8 ± 104.6 MPa/(g/cm^3) and specific stiffness of 100.4 ± 17.6 GPa/(g/cm^3). Relative to the pristine unprocessed material, these results represent a 205 % increase in specific strength and 1661 % increase in specific stiffness. As no plateau in specific stiffness or strength is apparent in Figure 4(b), it is possible that higher levels of pre-strain may lead to further improvements in mechanical properties.

To gain further insight into the relationship between CNT alignment and inter-tube bond formation, CNTs in a stacked, [0/90] perpendicular arrangement [Figure S1(b)] were simulated. CNTs in parallel alignment with each other, represented by the simulations discussed earlier, are prevalent within bundles, while CNTs misaligned with each other are expected between adjacent bundles. The experimental materials are understood to have an abundance of both parallel and misaligned CNTs within and between bundles, respectively. In the pristine

unstretched material the bundles are randomly oriented resulting in more misaligned CNTs, while stretching the material orients the bundles into closer alignment in the direction the stretch was applied. Comparing the parallel and perpendicular simulation geometries can help determine if misaligned CNTs impede the formation of covalent links.

The progression of structural changes is shown in Figure 4(c), and the corresponding phase diagram is reported in Figure 4(d). The formation of bonds at the side-loops, observed in the parallel CNT system, did not occur for the perpendicular CNTs. This was because the perpendicular CNTs cannot pack as tightly as the parallel tubes resulting in a small void located adjacent to the side-loops (Figure 4e), where the most reactive atoms are located. This may explain, in part, why the SPS process is more effective for increasingly aligned CNT material.

In Figure 5, the stretched and processed material in this work is compared to a few other representative CNT sheet processing methods from the literature. The specific strengths of the pristine and processed material from this work greatly exceed the fracture strength of loose-powder CNT compacts that have been SPS processed[29,31–34]. The improvements in properties reported in this work exceed what was reported for functionalized and irradiated CNT sheets[18] and stretched and hot-pressed CNT sheets,[45] and are similar to what was achieved by infusing with BMI resin and stretching up to 80%[8,9], despite only stretching up to 40% in this work. While no existing mature material formats are exactly comparable to the processed CNT sheets in this work, carbon fiber tows and aerospace IM7/8552 carbon fiber reinforced polymer composites are shown in Figure 5 for reference. The stretched and processed CNT sheet format is most similar to unidirectional IM7/8552, since both are aligned, while the unstretched sheets are more comparable to quasi-isotropic IM7/8552 since both are relatively isotropic in the in-plane directions. It is apparent that the quality of the pristine CNT sheet material influences the processed material properties. An important next step is improved control of the CNT manufacturing process to produce nanotube material with characteristics that the modeling and experiments in this work suggest are favorable for optimal covalent bond formation.

Summary

Introducing covalent links within densified and aligned CNT materials is an important step in improving the mechanical properties of commercially available CNT materials. In this work, combined pulsed electrical current, temperature, and pressure were applied to CNT sheets to introduce covalent linkages between the CNTs that affected their macroscale mechanical properties. In contrast to typical infiltration methods, these results show continued improvements in mechanical performance with increasing alignment and density in the starting material; the greatest improvements observed in this work were found in the most highly aligned sample.

These results demonstrate the capability of applying combined stimuli compatible with CNTs to improve mechanical performance. While large-scale production using this approach remains to be developed, this chemistry warrants further investigation, since this is a high-energy process which makes it difficult to closely control and optimize. While the results are challenging to interpret because the pulsed electrical current, temperature, and pressure are not independent quantities, the role of the pulsed current flow appears to be significant. With it, the applied pressures needed to form sp^3 hybridized structures between CNTs are lowered. However, the mechanisms responsible for this remain unresolved.

Acknowledgements

The authors thank Prof. Richard Liang and Dr. Jin Gyu Park (Florida State University) for the HR-TEM work. Computational resources supporting this work were provided by the NASA High-End Computing Program through the NASA Advanced Supercomputing Division at Ames Research Center.

References

1. Samareh, J. A. & Siochi, E. J. Systems analysis of carbon nanotubes: opportunities and challenges for space applications. *Nanotechnology* **28**, 372001 (2017).

2. Peng, B. *et al.* Measurements of near-ultimate strength for multiwalled carbon nanotubes and irradiation-induced crosslinking improvements. *Nat. Nanotechnol.* **3**, 626–631 (2008).

3. Lee, C., Wei, X., Kysar, J. W. & Hone, J. Measurement of the Elastic Properties and Intrinsic Strength of Monolayer Graphene. *Science* **321**, 385–388 (2008).

4. Kim, J.-W. *et al.* Assessment of carbon nanotube yarns as reinforcement for composite overwrapped pressure vessels. *Compos. Part A* **84**, 256–265 (2016).

5. Kinloch, I. A., Suhr, J., Lou, J., Young, R. J. & Ajayan, P. M. Composites with carbon nanotubes and graphene: An outlook. *Science* **362**, 547–553 (2018).

6. Janas, D. & Koziol, K. K. Carbon nanotube fibers and films: synthesis, applications and perspectives of the direct-spinning method. *Nanoscale* **8**, 19475–19490 (2016).

7. Cho, H. *et al.* Hierarchical structure of carbon nanotube fibers, and the change of structure during densification by wet stretching. *Carbon* **136**, 409–416 (2018).

8. Downes, R. D. *et al.* Geometrically constrained self-assembly and crystal packing of flattened and aligned carbon nanotubes. *Carbon* **93**, 953–966 (2015).

9. Jolowsky, C., Sweat, R., Park, J. G., Hao, A. & Liang, R. Microstructure evolution and self-assembling of CNT networks during mechanical stretching and mechanical properties of highly aligned CNT composites. *Compos. Sci. Technol.* **166**, 125–130 (2018).

10. Behabtu, N. *et al.* Strong, Light, Multifunctional Fibers of Carbon Nanotubes with Ultrahigh

Conductivity. *Science* **339**, 182–186 (2013).

11. Tasis, D., Tagmatarchis, N., Bianco, A. & Prato, M. Chemistry of Carbon Nanotubes. *Chem. Rev.* **106**, 1105–1136 (2006).

12. Sahoo, N. G., Rana, S., Cho, J. W., Li, L. & Chan, S. H. Polymer nanocomposites based on functionalized carbon nanotubes. *Prog. Polym. Sci.* **35**, 837–867 (2010).

13. Banhart, F. Irradiation effects in carbon nanostructures. *Reports Prog. Phys.* **62**, 1181 (1999).

14. Krasheninnikov, A. V. & Banhart, F. Engineering of nanostructured carbon materials with electron or ion beams. *Nat. Mater.* **6**, 723–733 (2007).

15. Krasheninnikov, A. V. & Nordlund, K. Ion and electron irradiation-induced effects in nanostructured materials. *J. Appl. Phys.* **107**, 71301 (2010).

16. Park, O.-K. *et al.* High-modulus and strength carbon nanotube fibers using molecular cross-linking. *Carbon* **118**, 413–421 (2017).

17. Jung, Y., Cho, Y. S., Lee, J. W., Oh, J. Y. & Park, C. R. How can we make carbon nanotube yarn stronger? *Compos. Sci. Technol.* **166**, 95–108 (2018).

18. Williams, T. S. *et al.* Trade-off between the Mechanical Strength and Microwave Electrical Properties of Functionalized and Irradiated Carbon Nanotube Sheets. *ACS Appl. Mater. Interfaces* **8**, 9327–9334 (2016).

19. Kim, J.-W. *et al.* Toward high performance thermoset/carbon nanotube sheet nanocomposites via resistive heating assisted infiltration and cure. *ACS Appl. Mater. Interfaces* **6**, 18832–18843 (2014).

20. Paci, J. T., Furmanchuk, A., Espinosa, H. D. & Schatz, G. C. Shear and friction between carbon nanotubes in bundles and yarns. *Nano Lett.* **14**, 6138–6147 (2014).

21. Jensen, B. D. *et al.* Simulating the effects of carbon nanotube continuity and interfacial bonding on composite strength and stiffness. *Compos. Sci. Technol.* **166**, 10–19 (2018).

22. Hod, O., Meyer, E., Zheng, Q. & Urbakh, M. Structural superlubricity and ultralow friction across the length scales. *Nature* **563**, 485–492 (2018).

23. Orrù, R., Licheri, R., Locci, A. M., Cincotti, A. & Cao, G. Consolidation/synthesis of materials by electric current activated/assisted sintering. *Mater. Sci. Eng. R Reports* **63**, 127–287 (2009).

24. Li, J. L., Bai, G. Z., Feng, J. W. & Jiang, W. Microstructure and mechanical properties of hot-pressed carbon nanotubes compacted by spark plasma sintering. *Carbon* **43**, 2649–2653 (2005).

25. Yang, K. *et al.* Inter-tube bonding, graphene formation and anisotropic transport properties in spark plasma sintered multi-wall carbon nanotube arrays. *Carbon* **48**, 756–762 (2010).

26. Hojati-Talemi, P., Kannan, A. G. & Simon, G. P. Fusion of carbon nanotubes for fabrication of field emission cathodes. *Carbon* **50**, 356–361 (2012).

27. Ozden, S. *et al.* Controlled 3D Carbon Nanotube Structures by Plasma Welding. *Adv. Mater. Interfaces* **3**, 1–8 (2016).

28. Yang, K. *et al.* Tuning electrical and thermal connectivity in multiwalled carbon nanotube buckypaper. *J. Phys. Condens. Matter* **22**, 334215 (2010).

29. Wang, W. *et al.* Preparation and characteristics of a binderless carbon nanotube monolith and its biocompatibility. *Mater. Sci. Eng. C* **28**, 1082–1086 (2008).

30. Cha, S. I. *et al.* Mechanical and electrical properties of cross-linked carbon nanotubes. *Carbon* **46**, 482–488 (2008).

31. Yamamoto, G. *et al.* Single-walled carbon nanotube-derived novel structural material. *J. Mater. Res.* **21**,

1537–1542 (2006).

32. Sato, Y. *et al.* Influence of the structure of the nanotube on the mechanical properties of binder-free multi-walled carbon nanotube solids. *Carbon* **50**, 34–39 (2012).

33. Zhang, Z.-H., Qi, L., Shen, X.-B., Wang, F.-C. & Lee, S.-K. Microstructure and mechanical properties of bulk carbon nanotubes compacted by spark plasma sintering. *Mater. Sci. Eng. A* **573**, 12–17 (2013).

34. Yamamoto, G. *et al.* Preparation of single-walled carbon nanotube solids and their mechanical properties. *J. Mater. Res.* **20**, 2609–2612 (2005).

35. Downes, R., Wang, S., Haldane, D., Moench, A. & Liang, R. Strain-Induced Alignment Mechanisms of Carbon Nanotube Networks. *Adv. Eng. Mater.* **17**, 349–358 (2015).

36. Chopra, N. G. *et al.* Fully collapsed carbon nanotubes. *Nature* **377**, 135–138 (1995).

37. van Duin, A. C. T., Dasgupta, S., Lorant, F. & Goddard III, W. A. ReaxFF: A reactive force field for hydrocarbons. *J. Phys. Chem. A* **105**, 9396–9409 (2001).

38. Goverapet Srinivasan, S., van Duin, A. C. T. & Ganesh, P. Development of a ReaxFF potential for carbon condensed phases and its application to the thermal fragmentation of a large fullerene. *J. Phys. Chem. A* **119**, 571–580 (2015).

39. Haddon, R. C. Chemistry of the Fullerenes: The Manifestation of Strain in a Class of Continuous Aromatic Molecules. *Science* **261**, 1545–1550 (1993).

40. Vilatela, J. J., Deng, L., Kinloch, I. A., Young, R. J. & Windle, A. H. Structure of and stress transfer in fibres spun from carbon nanotubes produced by chemical vapour deposition. *Carbon* **49**, 4149–4158 (2011).

41. Zhang, F. *et al.* Conversion of carbon nanotubes to diamond by spark plasma sintering. *Carbon* **43**,

1254–1258 (2005).

42. Jha, S. K. *et al.* The effects of external fields in ceramic sintering. *J. Am. Ceram. Soc.* **102**, 5–31 (2019).

43. Zhang, F., Mihoc, C., Ahmed, F., Lathe, C. & Burkel, E. Thermal stability of carbon nanotubes, fullerene and graphite under spark plasma sintering. *Chem. Phys. Lett.* **510**, 109–114 (2011).

44. Dresselhaus, M. S., Jorio, A., Souza Filho, A. G. & Saito, R. Defect characterization in graphene and carbon nanotubes using Raman spectroscopy. *Philos. Trans. R. Soc. A Math. Phys. Eng. Sci.* **368**, 5355–5377 (2010).

45. Liu, Q. *et al.* Highly aligned dense carbon nanotube sheets induced by multiple stretching and pressing. *Nanoscale* **6**, 4338–4344 (2014).

46. Plimpton, S. Fast Parallel Algorithms for Short – Range Molecular Dynamics. *Jounal Comput. Phys.* **117**, 1–19 (1995).

47. Aktulga, H. M., Fogarty, J. C., Pandit, S. A. & Grama, A. Y. Parallel reactive molecular dynamics: Numerical methods and algorithmic techniques. *Parallel Comput.* **38**, 245–259 (2012).

48. Stukowski, A. Visualization and analysis of atomistic simulation data with OVITO–the Open Visualization Tool. *Model. Simul. Mater. Sci. Eng.* **18**, 015012 (2009).

49. Maras, E., Trushin, O., Stukowski, A., Ala-Nissila, T. & Jónsson, H. Global transition path search for dislocation formation in Ge on Si(001). *Comput. Phys. Commun.* **205**, 13–21 (2016).

50. Mirzaei, A. *et al.* Surprising synthesis of nanodiamond from single-walled carbon nanotubes by the spark plasma sintering process. *Electron. Mater. Lett.* **12**, 747–752 (2016).

51. Zhang, F., Adam, M., Ahmed, F., Otterstein, E. & Burkel, E. Pulsed electric field induced diamond synthesis from carbon nanotubes with solvent catalysts. *Diam. Relat. Mater.* **20**, 853–858 (2011).

52. Marks, N. A. Generalizing the environment-dependent interaction potential for carbon. *Phys. Rev. B* **63**, 35401 (2000).

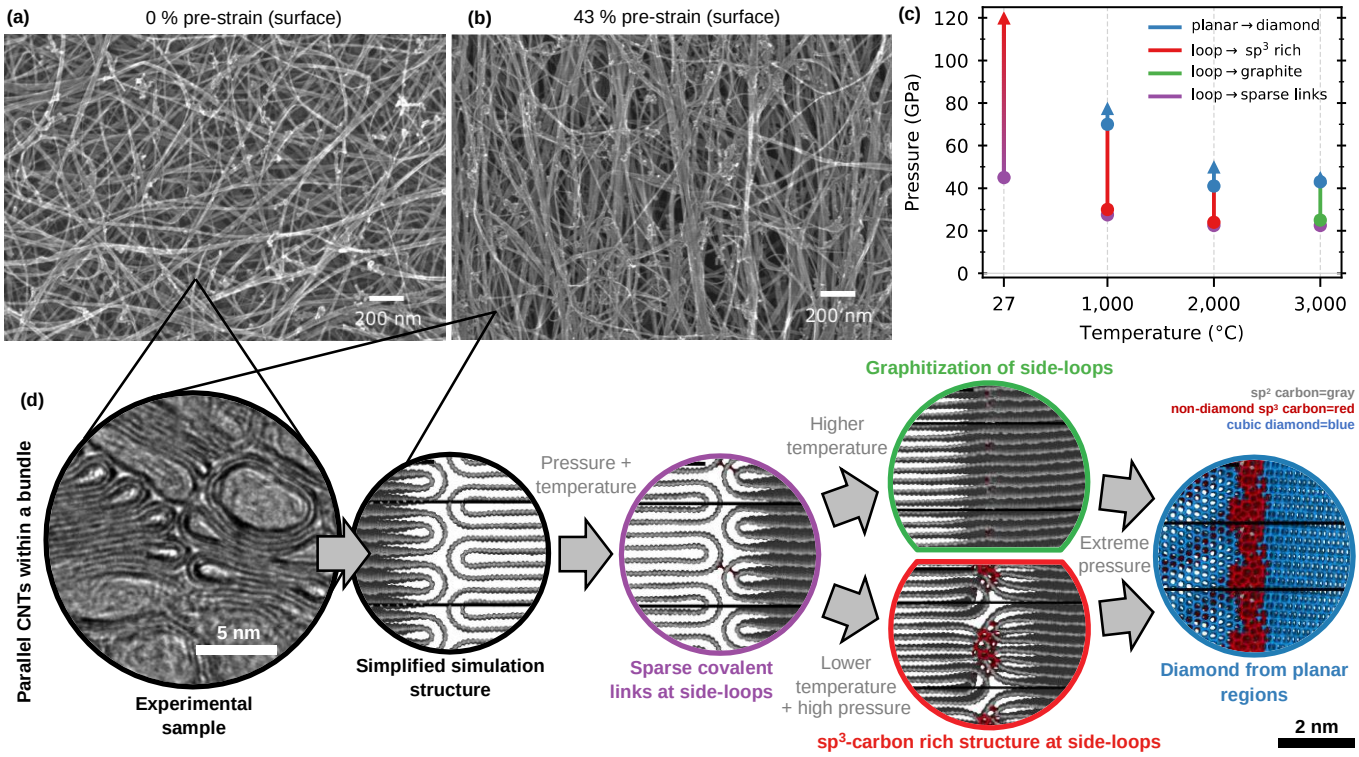

Figure 1. SEM micrographs of (a) pristine and (b) pre-strained CNT sheets. (c) Simulated phase diagram for parallel CNTs. The gradient in the 27 ˚C isotherm indicates a gradual increase in covalent bonding without a clear distinction between sparse covalent bonding and sp^3-carbon rich structures. Arrows indicate the highest simulated conditions. (d) Simulated structural outcomes after returning to ambient pressure and temperature for parallel CNTs.

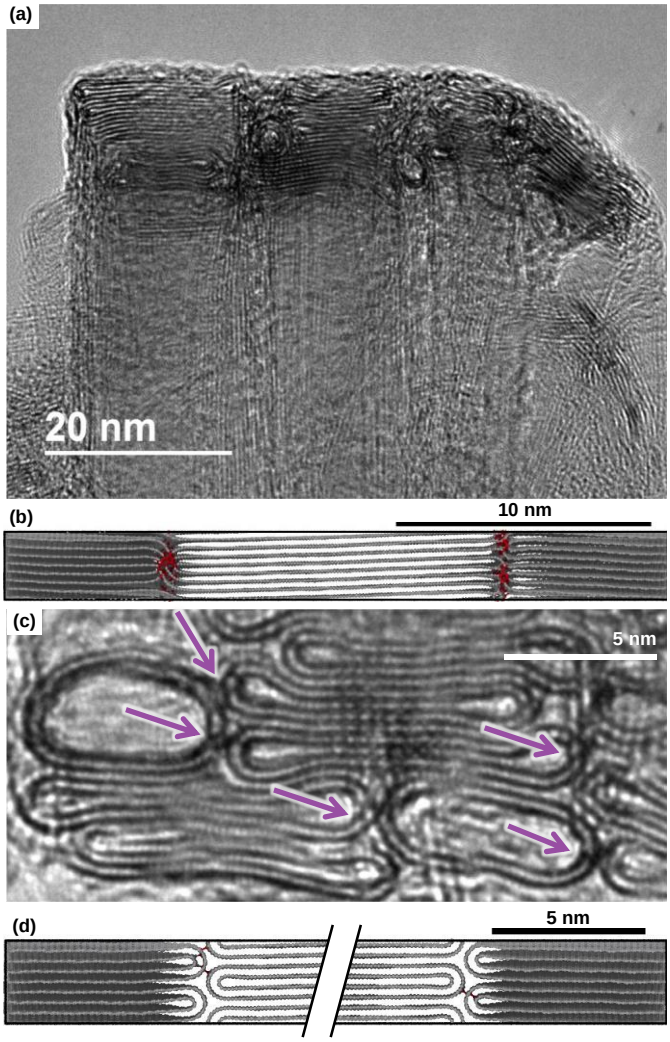

Figure 2. (a) HR-TEM image of CNT structure after SPS processing at 1,000 ˚C and 20 MPa. (b) Example of an sp^3-carbon rich structure from the simulations (quenched structure after 2,000 ˚C, 40 GPa). (c) Zoomed HR-TEM of image at another location showing CNT spacing less than the van der Waals distance (arrows) at higher curvature locations and (d) a simulation image for comparison, having sparse covalent linking reducing the CNT-CNT distance (quenched structure after 2,000 ˚C, 25 GPa). The simulation has been scaled to match the HR-TEM scale-bar.

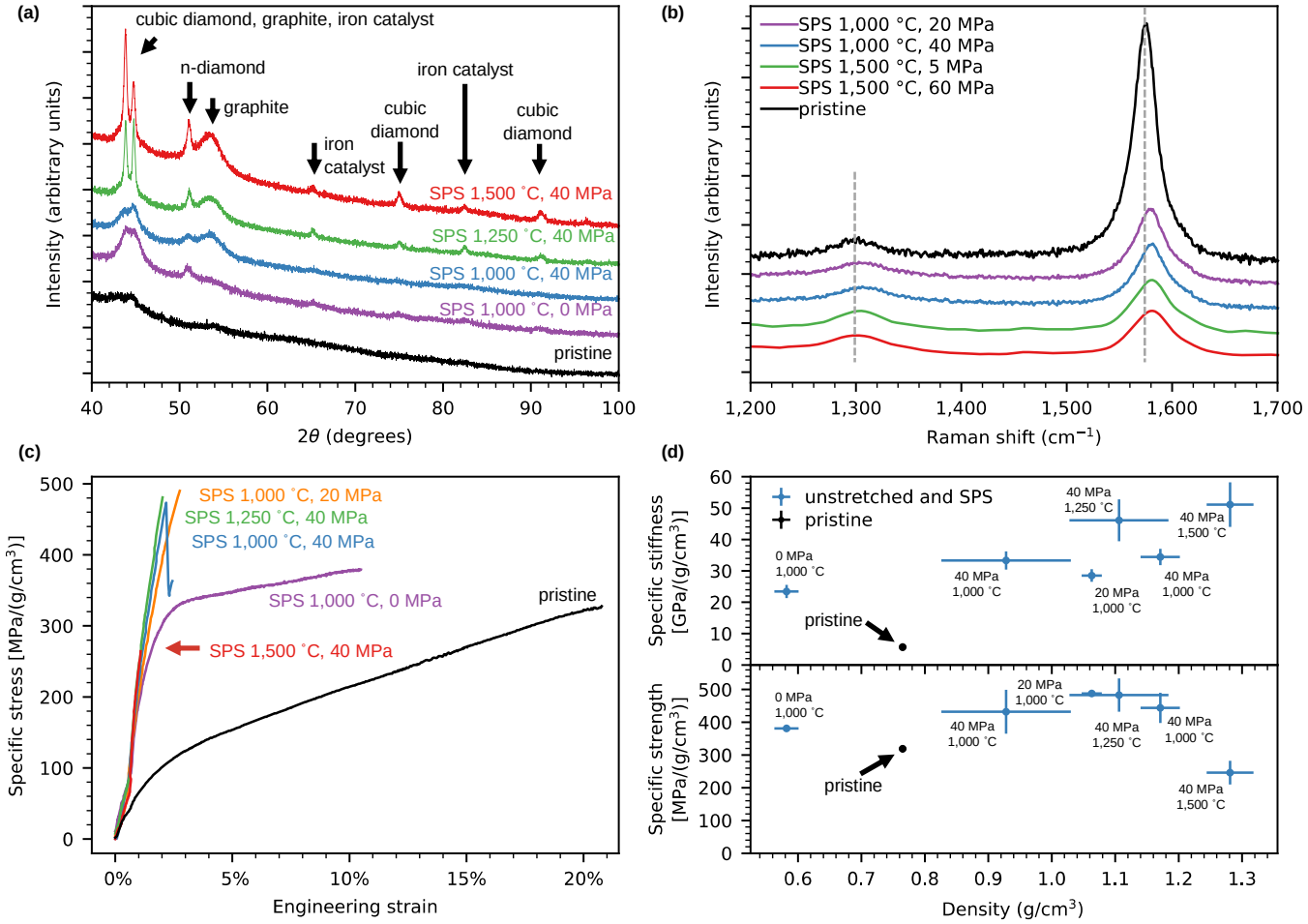

Figure 3. (a) XRD diffraction spectra of 0 % pre-strained samples processed at various SPS processing temperatures and pressures. (b) Raman spectra of 0 % pre-strained CNT sheets processed under various SPS pressures and temperatures. (c) Representative stress-strain responses of 0 % pre-strained CNT sheets processed under various SPS pressures and temperatures. (d) Specific stiffness and strength of 0 % pre-strained CNT sheets plotted against density after SPS processing. Error bars indicate the standard deviation over five samples. For some samples, error bars are smaller than the symbol size.

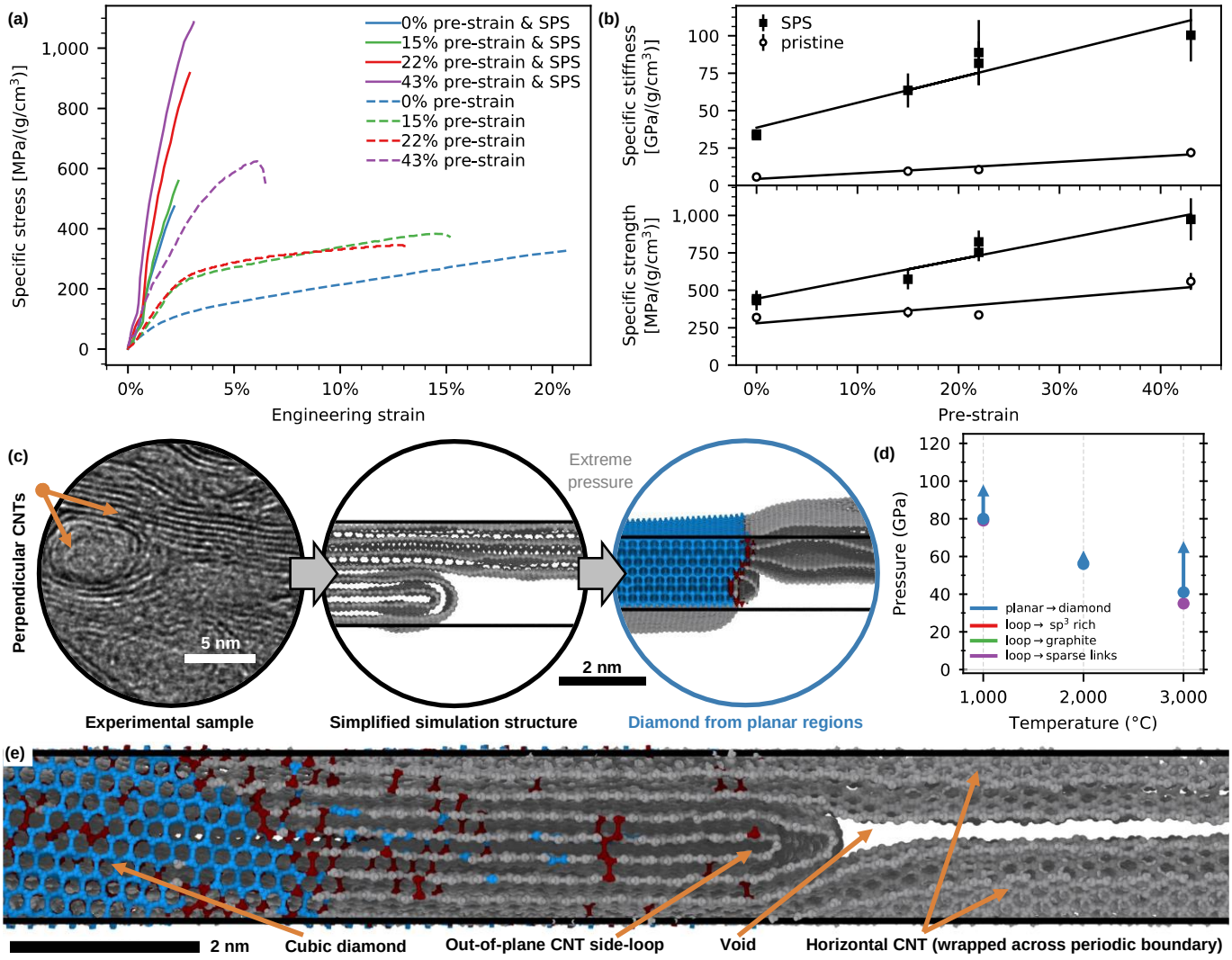

Figure 4. (a) Representative stress-strain responses of pre-strained CNT sheets with and without SPS processing. SPS samples were processed at 40 MPa and 1,000 ˚C. (b) Specific stiffness and strength as a function of pre-strain. Error bars indicate the standard deviation over five samples. For some samples, error bars are smaller than the symbol size. (c) Simulated structural outcomes for low-packed perpendicular systems. (d) Simulated phase diagram for perpendicular systems. Arrows indicate the highest simulated conditions. (e) Void space adjacent to the side-loop of simulated perpendicularly misaligned CNTs while compressed at ~56 GPa and 2,000 ˚C.

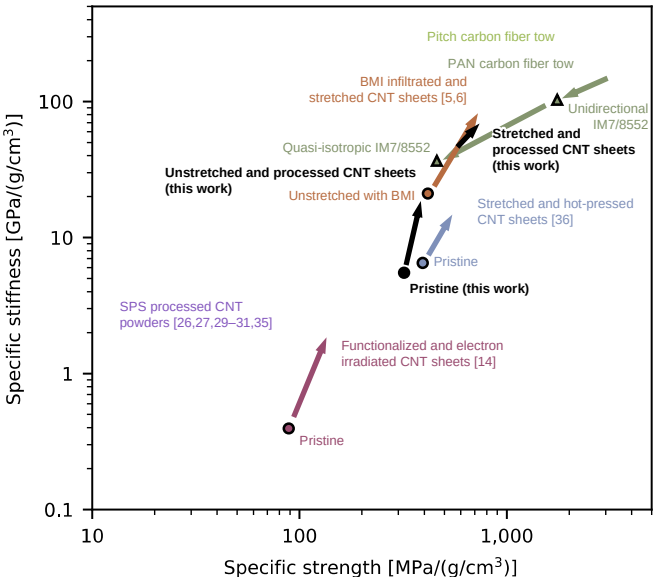

Figure 5. Ashby plot comparing stretched and processed CNT sheet from this work to CNT sheet processes in the literature, SPS processed CNT powders, and carbon fiber constituents and composites. All specific strengths are tensile, except SPS processed CNT powders, which were from 3-point bending tests.

SUPPLEMENTAL INFORMATION:

Materials and methods

Simulation methods

Molecular dynamics simulations were performed using the open-source Large-scale Atomic/Molecular Massively Parallel Simulator (LAMMPS) software.[46,47] The reactive force field ReaxFF with the ReaxFF$_{C\text{-}2013}$ parameters was used.[37,38] Simulation structures were rendered using the Ovito software.[48] The coordination of the atoms was determined by counting the number of atoms within a cutoff distance of 0.18 nm, which corresponds to the zero density point in the radial distribution function separating first and second neighbors. Cubic diamond structures were identified based on the location of an atoms neighbor relative to the cubic diamond lattice points, as implemented in the Ovito software.[49] All systems used periodic boundary conditions in all three directions. All CNTs had an inner diameter of ~8 nm before they were collapsed. All parallel

systems contained four CNTs, and perpendicular systems had two CNTs. The chirality of the parallel CNT system was mixed with alternating columns of armchair and zigzag. The chirality of the CNTs in the perpendicular systems were one armchair and one zigzag. Because the CNTs are arranged in a perpendicular configuration, the crystal lattice is oriented in the same direction at the junction. All systems contain ~120,000 atoms.

Pressures were increased along isotherms at 27 (room temperature), 1,000, 2,000, and 3,000 ˚C. A Langevin thermostat and Nose-Hoover barostat were used in all simulations for temperature and pressure control. Pressure was controlled independently along the two transverse directions while the pressure was maintained at zero along the axial direction for the parallel CNTs. For the perpendicular CNT setups, both axial directions were maintained at zero pressure while the pressure was controlled in the direction normal to the junction. Because the overlapped junction area of the perpendicular CNTs compromised 17 % of the cross section of the total box, barostat target pressures were set to 17 % of the desired junction pressure, which resulted in the appropriate junction pressures. A time step of 0.2 fs was used in most cases. A few of the high temperature isotherms were repeated with a time step of 0.1 fs to ensure the time step was sufficiently small. For the perpendicular CNT setup, the system was divided into ~2,550 subvolumes within which the pressure was computed using the subdomain virial stress and volume. The junction pressure was computed from the average pressure in the subdomains comprising the junction. Pressures were increased at a rate of 50 GPa/ns for most simulations. In the 27 ˚C simulations and the 1,000 ˚C perpendicular simulations, a portion of the simulation was performed at a rate of 500 GPa/ns to improve computational efficiency over a large pressure range. In a few cases, a ramp rate of 500 GPa/ns was also used between pressures where no changes to the material were expected or observed. Snapshots at 5 GPa intervals were saved and quenched to room temperature and pressure in 10 ps, and then held for 10 ps. This was done so structures could be compared to experimental samples characterized at room temperature and pressure after the SPS process. At high temperatures a variety of transient covalent bonds were observed and the quenching process was used to identify the stability of these bonds, most of which did not persist after the quenching process.

The pressures and temperatures of these nano-scale simulations were intended to represent local domains within the experimental material that experience pressures and temperatures much higher than those nominally applied during the SPS process. These simulations operated under the assumption that the experimentally observed diamond particles form in these high-pressure and high-temperature regions, consistent with the phase diagram for carbon, and not through other specialized conditions such as those required for atmospheric pressure CVD diamond growth. The simulations considered direct conversion of CNTs to other solid forms, and not to other intermediary phases such as liquid carbon, gaseous carbon, or highly-strained many-layered nano-onions, although some have speculated in the literature that this may occur in the SPS process.[41,50,51] The energy of compressed graphite and diamond were explicitly included in the training set of the $ReaxFF_{C\text{-}2013}$ parameters. However, the phase-change energy barriers were not explicitly included in the ReaxFF training set. Some preliminary tests indicated that $ReaxFF_{C\text{-}2013}$ parameters predict a higher graphite to diamond energy barrier (11.5 kcal/mol) than DFT (7.6 kcal/mol).[52] Finally, it is important to note that the pressures and temperatures in the simulations occur over nano-scale domains. Therefore, relating the local simulation pressures and temperatures to globally reported values such as those from high-pressure, high-temperatures diamond anvil cell experiments will require consideration of the effects of the material microstructure.

Experimental methods

As-received acetone densified CNT sheet (Nanocomp Technologies, Inc., Lot#: 151-92, areal density of 14.67 g/m^2) was used to fabricate SPS processed samples. The CNT sheet contained mostly double-walled CNTs with average diameters of 7 ~ 8 nm. The CNT sheets contain ~10 wt.% residual iron catalyst particles from the floating catalyst manufacturing process. A large fraction of the tubes was observed to be collapsed in the CNT sheets using HR-TEM. For the pre-strained samples, the sheet (76 × 178 cm) was clamped on a custom-built stretcher between two metal bars and then mechanically stretched to the desired level of stretching (from 0 to 43 %) driven by a stepper motor. Acetone solvent (Sigma-Aldrich) was applied during the stretching step for the 22 and 43 % strain samples. The level of pre-strain was calculated using length differences of marked lines (7.62 cm gap) at the center of the sheet before and after stretching. After stretching, the sample was cut from the

center of the sheet (within the marked lines) and then stored under ambient conditions. Circular samples of 1 cm diameter were used for Raman and HR-TEM characterization, while larger 5.08 × 5.08 cm square samples were used for mechanical and XRD characterization. The cut and pre-stained CNT sheet samples were sandwiched between graphite dies in the SPS chamber of a GT SPS system (SPS25-10). SPS temperatures ranged from 1,000 to 1,500 ˚C and applied pressures ranged from 0 to 60 MPa, under an argon environment. The temperature of the graphite dies was monitored with an imbedded thermocouple and with an optical pyrometer through a window in the graphite die. The processing time for all samples was 5 min. During the process, the current and voltage was maintained at ~ 900 A and less than 5 V, respectively, with a 5 ms duration off period between each pulse. The heating rate was set to 100 ˚C/min.

Room temperature tensile properties of the pristine and pre-strained CNT sheets, with and without SPS processing, were determined using a Gatan Microtester 200 stage and Deben controller equipped with a 200 N load cell. The tensile testing method was based on ASTM standard D1708. The gauge length and cross head speed were 10 mm and 0.5 mm/min, respectively. The tensile specimens were rectangular strips with a width of 5 mm and length of 20 mm. Five specimens were tested to determine tensile strength and modulus for each SPS condition. Specific tensile stress was calculated by dividing the measured force (N) by the linear density (g/km) of each specimen, to eliminate measurement errors associated with sample thickness and specimen dimensions. The specific modulus was obtained from linear regression of the slope between 100 and 200 MPa/(g/cm^3) of the stress-strain curve for SPS processed samples. The specific modulus of pristine samples was calculated from the slope between 10 and 30 % of the ultimate tensile stress to eliminate the initial lag in stress-strain behavior. The sample thickness was determined using a digital thickness gauge (Mitutoyo Corp., Model ID-S112PE). The nominal density was determined by measuring the length, width, thickness, and weight of the specimen.

High resolution transmission electron microscopy (HR-TEM) was conducted using a Joel JEM-ARM200cF system (a sub-Angstrom Cs corrected transmission/scanning transmission microscope) at an acceleration voltage of 80 keV to minimize beam damage of the CNTs. Cross-sectional HR-TEM samples were prepared using a focused ion beam (FIB, FEI Helios 600) system equipped with a precise positioning stage

(OmniProbe^{TM}). The sample thickness was generally less than 30 nm and CNTs were aligned at nearly 90 degrees to the manufacturing direction of CNT sheet. Note that the CNTs in the as-received sheet were mostly randomly oriented before stretching, however, there was a small degree of pre-existing directionality present as a result of the manufacturing process. All mechanical tests and stretching were conducted along this manufacturing alignment direction. X-ray diffraction analyses were conducted on a Rigaku SmartLab x-ray diffractometer with a Cu Kα radiation source. Raman spectra were acquired with an excitation wavelength of 785 nm on a Thermo-Nicolet-Almega Dispersive Raman Spectrometer through a 100 μm pinhole. The acquisition of each spectrum consisted of 5 scans.

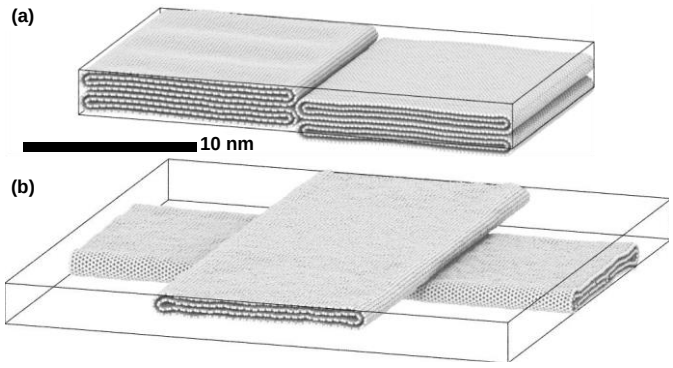

Figure S1. Starting simulation structures for (a) parallel and (b) perpendicularly aligned double-wall CNTs.